This is a post-peer-review, pre-copyedit version of an article published in International Journal of Precision Engineering and Manufacturing-Green Technology**. The final authenticated version is available online at:** https://dx.doi.org/10.1007/s40684-020-00296-2

Postprint of: Szkodo, M., Bień, A. & Stanisławska, A. Laser Beam as a Precision Tool to Increase Fatigue Resistance in an Eyelet of Undercarriage Drag Strut. *Int. J. of Precis. Eng. and Manuf.-Green Tech.* (2021) DOI: 10.1007/s40684-020-00296-2

Laser beam as a precision tool to increase fatigue resistance in an eyelet of undercarriage drag strut

Marek Szkodo [1]*, Anna Bień[2], Alicja Stanisławska[1]

[1] Gdańsk University of Technology, Mechanical Engineering Faculty, Gdansk, G. Narutowicza 11/12, 80-233 Gdańsk, Poland
[2] Geoengineering Faculty, University of Warmia and Mazury in Olsztyn**,** Heweliusza 4, 10-724 Olsztyn, Poland
* correspondence mszkodo@pg.edu.pl

Abstract: The article contains the results of tests on a laser-processed eyelet of undercarriage drag strut to increase its fatigue strength. Laser processing concentrated on both sides around the hole of eye for connecting the undercarriage drag strut caused that the material in this area withstood more than twice the number of load cycles established for this material. In order to determine the reasons for the increase in fatigue strength, residual stresses in laser-treated LT areas and in the base metal BM located between melted paths were determined, using the nanoindentation test and Williamson Hall method. The modified Williamson Hall analysis of XRD patterns was also used to determine the dislocation density in both areas. The results indicate that high residual tensile stresses occur in melted areas and in base metal located between melted paths occur high residual compressive stresses. A large increase in hardness and elastic properties, dissolution of non-metallic inclusions, as well as large solid solution and sub-grain strengthening contributed to the high fatigue resistance of the melted areas.

Keywords: laser treatment; fatigue; ultra-high strength steel; residual stress; nanoindentation test; Williamson Hall analysis

1. Introduction

Laser beam is a chemically clean light source and it is used to form the properties of the processed surface layer. Rapid heating and subsequent rapid cooling of the processed material induces the transformation of the microstructure and surface properties are altered. Compared to classic hardening, laser hardening does not require the use of toxic coolants that have a negative impact on the natural environment. The use of laser hardening also solves the problem of utilization of used coolants, which significantly reduces the cost of production. The use of a laser beam enables also selective hardening of surfaces, which shortens the production time and the amount of energy necessary to produce the element. Due to these benefits, lasers are more and more commonly used to manufacture machine and device components [1-3]. In addition, laser machining generates residual stresses in the workpiece. There are many literature reports

describing the beneficial effects of laser processing on the fatigue of different steel grades. For example, Černy and Sis report in their work [4] that laser hardening causes significant beneficial effects of compressive stresses induced by laser processing on fatigue resistance of 42CrMo4 steel. However, they did not provide residual stress values or their distribution in the investigated sample. According to them, laser processing caused retardation or arrest of short fatigue cracks emanating from microstructure defects such as inclusions. Božić et al. [5] simulated the development of fatigue cracks using the finite element method. They reported the simulated crack growth rate was relatively higher in the region of tensile residual stresses and lower where compressive residual stresses prevail. In turn, McDaniels et al. [6] showed that the increase in fatigue resistance of AISI 4340 steel after laser alloying is mainly caused by dissolving inclusions and forming a fine-grained microstructure in the heat affected zone. The influence of laser hardening on plane bending fatigue behavior of a B–Mn SS2131 steel has been also studied by De la Cruz et al. [7]. They spirally re-melted the workpiece surfaces with overlapping tracks. According to them, laser hardening improves the fatigue limit of quenched and tempered smooth and notched specimens by 18 and 56% respectively. The detrimental factors that occur with laser hardening are the formation of soft surface layers and low compressive residual stresses at the overlapping zones. There are also reports that laser hardening does not improve fatigue resistance or that it even reduces this resistance due to the generation of tensile stress. For example Bergmann [8] reports a decrease in the fatigue limit of a laser surface-melted ferritic iron. All the above-mentioned results refer to fatigue tests carried out on the samples. Relatively few reports concern tests of fatigue resistance of specific machine and equipment parts after laser processing [9-11]. For example, Walker et al. [9] and Lourenço et al. [10] proposed a novel repair technique employing laser cladding. They reported a study of the fatigue endurance of AerMet100 steel components repaired by the laser cladding process. The fatigue test results showed that the crack propagation lines from a common initial depth of 0.25 mm for the as-clad samples were significantly longer than the baseline samples by a factor of three to four. The average fatigue life of the as-clad specimen was improved significantly to 184,290 cycles, as compared to the as-damaged baseline condition of 16,087 cycles [9]. According to them, the longer fatigue life is attributed to the beneficial compressive residual stresses resulting from the repair process.

From the reports cited above, it seems that fatigue behaviour depends mainly on the residual stress distribution produced by the surface treatment. However, the values and distribution of residual stress after laser processing will depend on the parameters of the laser treatment and the size and shape of the workpiece. In addition, proper design and the arrangement of melted paths on the surface of the workpiece can contribute to an increase in fatigue resistance by generating favourable stresses in the base material between the melted paths. There are few reports in the literature describing the distribution of residual stresses in areas of material with unchanged microstructure, located between melted paths. The scientific objective of the study is to determine how the state of residual stress and mechanical properties after laser re-melting affect the initiation of fatigue cracks in the eyelet of undercarriage drug strut made of a high strength martensitic steel. In order to determine residual stress in melted material, in heat

affected zone and in base metal being between melted paths, two methods were used: nanoindentation test and XRD pattern analysis by Williamson-Hall method. This work contributes to understanding the reasons for increasing the fatigue resistance of laser processed a high strength martensitic steel and it provides essential results on the overall potential of laser treating as a future solution for aircraft landing gear.

2. Materials and Methods

2.1. Object of investigation

The drag strut was made of ultra-high strength 30HGSNA steel. 30HGSNA steel is a material used widely in modern aircraft structure, particularly in critical applications such as landing gears. Chemical composition of steel from which drag struts were produced is presented in Table 1. Tensile strength of the steel is 1700 ± 100 MPa and its yield point is 1520 MPa after following heat treatment:

Table 1. Chemical composition of 30HGSNA steel used to produce drag struts.

alloy	C	Mn	Si	Cr	Ni	Cu	P	S	Fe
30HGSNA	0.30	1.15	1.10	1.05	1.65	0.25	0.030	0.025	rest

isothermal hardening from 900 °C and double tempering, first at a temperature of 280 °C/3h and second one at 270 °C/3h. After tempering, the drag struts were cooled in air. After the heat treatment, the hardness of the steel ranged from 5.6 GPa to 6.1 GPa. Then, the surfaces of the drag struts underwent phosphatising. After this process iron phosphates are formed on the surface of the drag strut. Phosphate coating thickness ranges from 3 μm to 5 μm. Fig. 1 shows the shape and dimensions of the drag strut. Drag strut consists of two parts: the main part of drag strut made of seamless tube with a wall thickness of 6.5 mm and the eyelet. The main part of drag strut was welded to the eyelet by means of butt weld as presented in Fig. 1.

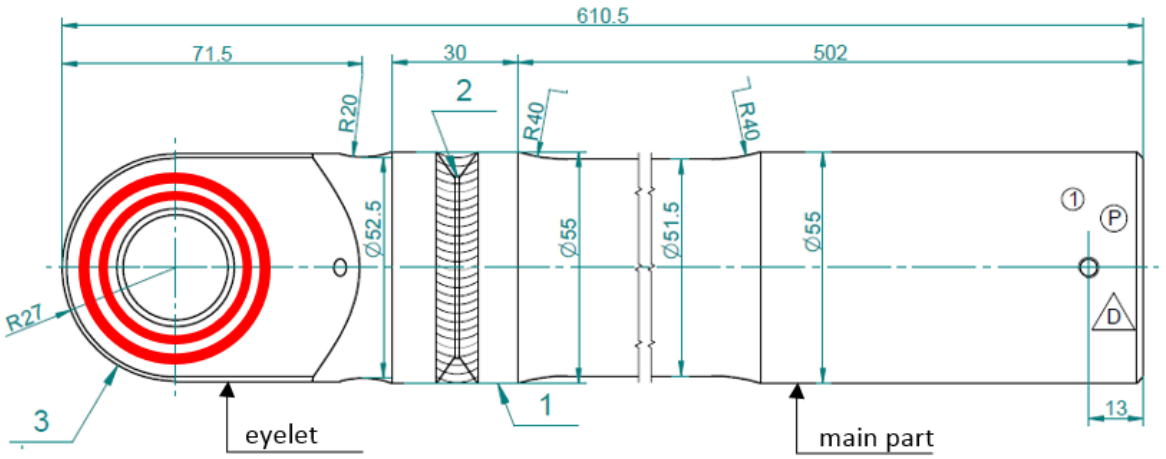

Fig. 1. Shape and dimensions of the drag strut used for testing. Red areas indicate melted paths.

2.2. Laser beam treatment

One of the drags strut was subjected to laser treatment. Two re-melted paths were made in the form of concentric circles around the eyelet hole. Their diameters were 39 mm and 47 mm, respectively, and their arrangement is shown in Fig. 1.The 39 mm diameter path was made clockwise, while the 47 mm path was melted counter clockwise. The starting point of the path coincides with the end point of the path. The same laser treatment was performed on the other side of the eyelet. The laser processing parameters for the treatment of the drag strut were as follows: laser type - CO_2; laser mode - pulse TEM_{10}; laser power - P = 900 W; radius spot laser - r = 1.5 mm; the speed of the laser beam - v = 3.5 mm/s; shielding gas - argon. The amount of energy delivered by the laser beam to the workpiece was selected on the basis of our earlier experiments by optimizing the thickness of the re-melted layer. The results of our previous studies concerning the phenomenon of blocking the fatigue crack propagation due to laser treatment, are described in [11-13].

2.3. Fatigue test

After laser processing, the fatigue test of the laser treated drag strut was performed. The result was compared with the effect of the fatigue tests with the same parameters carried out on the drag strut with no laser treatment. The fatigue tests were performed on the testing machine MTS 8502 (Instron) in the Air Force Institute of Technology in Warsaw. The drag struts were tested by axial cycling in laboratory environment at the stress ratios R (the minimum stress to the maximum stress) from 0 to -∞. The stress ratio was 0 for 880 cycles and R was -∞ for 70 cycles in each stage. The load frequency was 0.85 Hz. On one end, the drag strut was fixed in the testing machine by the eyelet of the drag strut and on the other end by the eye bolt screwed into the drag strut. MTS 8502 was equipped with the head whose force range equals ± 250 kN. The instantaneous values of the loading force and elongation of drag strut were recorded during the fatigue tests. One segment of load, consisting of 950 different cycles, represented all loads during one aircraft landing. 32 stages of loads occurred in one segment. The maximum magnitude of the force in each segment of the load was F = 195.4 kN and the minimum was F = - 19.54 kN. Graphical form of the segment of load program is shown in Fig. 2.

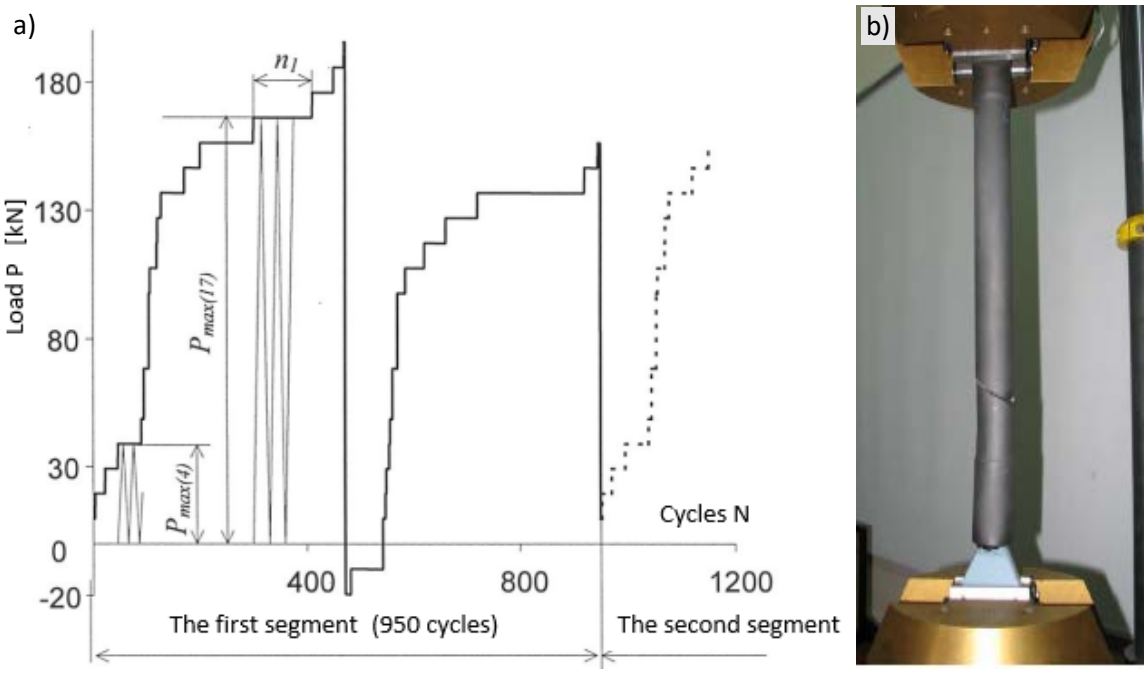

Fig. 2. The segment of load program occurring during the fatigue test – a) and the fatigue test device with sample clamped on – b).

The rate of the change of the loadings was constant during the fatigue tests and it was 200 kN/s. The duration of one program of the segment of load was 18.56 min. The temperature during the test ranged between 20-25 °C and air humidity was 40% to 60%. More details about fatigue tests can be found in our previous work [11].

2.4. Material characterization

Metallographic examination was performed on the cross section of the laser processed eyelet of drag strut using a scanning electron microscope (SEM, JOEL JSM-7800F) equipped with X-ray energy dispersive spectroscopy (EDS) analyser. Metallographic investigations were carried out on parts of the sample within the melted zone LT, in heat affected zone HAZ and in base material BM. Metallographic sample was cut as shown in Fig. 3. Before metallographic examination, sample was ground and polished to obtain an ultra-smooth surface. Energy dispersive spectroscopy (EDS) analysis was performed in order to identify the precipitates in

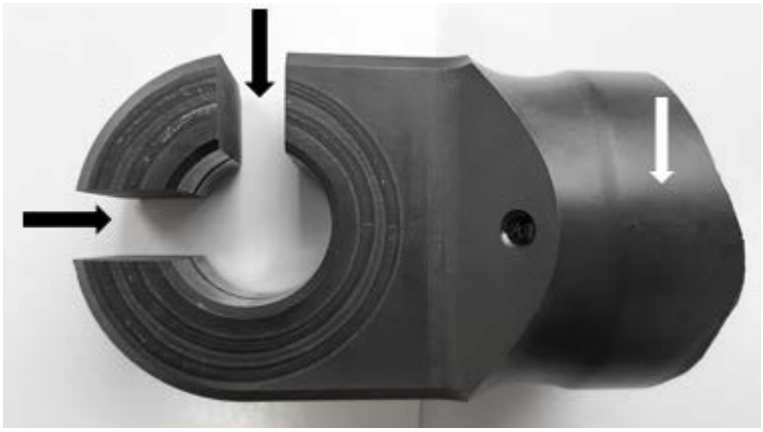

Fig. 3. Eyelet of drag strut. Place of sampling depicted by black arrows. White arrow indicates a cylindrical part of the eyelet of drag strut with no laser treatment.

the microstructure. Transmission electron microscopy (TEM, JOEL JEM-1400Plus) was also used for structural examinations. Structural observations were carried out using the thin films. Microscopic examination was performed at the accelerating voltage of 45 kV. The surface layer before and after laser remelting was also examined with the aid of X-ray diffractometer (XRD, with Cu Kα radiation λ=0.15418 nm), operated at 30 kV and 50 mA. This resulted in a spot size on the sample of 1 mm diameter and a penetration depth of 10 μm. Bragg–Brentano focusing geometry was used to collect diffraction patterns over the 2θ range from 15° to 90° with a step size of 0.004° and counting time of 30 s per step. Instrumental broadening effects were evaluated and corrected using a silicon standard. The X-ray diffraction patterns were evaluated by the convolutional multiple whole profile (CMWP) fitting procedure. In CMWP, the peak profile functions are calculated as the convolution of the size, strain, and instrumental broadening. The measured diffraction pattern is then fitted with the calculated profile function using a nonlinear least-squares method. Williamson-Hall plot was used to estimate the size of crystallites and microstrain in the analysed surface areas.

The hardness tests of the material were performed after the fatigue investigation, using NanoTest Vantage nanoindenter. This test was performed to determine the quantitative residual stresses in the melted paths, in the heat-affected zones (HAZ) and in the unprocessed materials. Residual stress was measured on the cross section of the drag strut. On the cross section, hardness test was made along two lines, normal to the surface, as shown in the Fig. 4, at the distance from surface ranging from 15 μm to 915 μm. “Line 1” included: area of the material melted by laser beam, the area of the heat affected zone and the raw material respectively. In

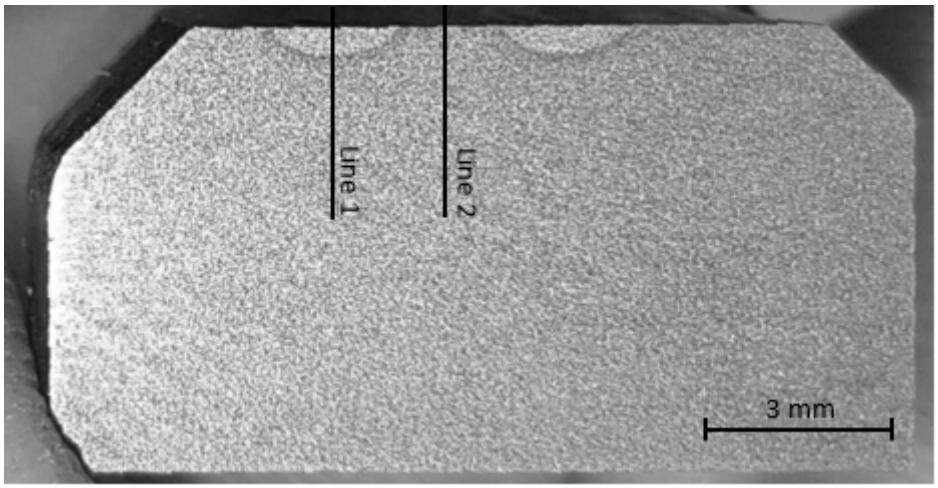

Fig. 4. Cross section view with marked measuring lines along which the stresses were determined.

turn “Line 2” included only raw material between two melted paths. Hardness tests were performed with a constant depth of the indenter penetration equal to 1450 nm. Berkovitch indenter was used for the hardness investigations. Loading and unloading rates were 50 mN/s. Indentation contains one cycle with 5 s dwell at maximum load. To obtain the residual stresses profiles from the surface, up to 15 μm deep into the material, a multiple load cycle with increasing load experiment was also done using nanoindenter NanoTest Vantage. Minimum load was 100 mN and maximum load was 20 N. Loading and unloading rates were 50 mN/s. Indentation contains 10 cycles with 5 s dwell at maximum load. Quantitatively, the residual stresses were determined by the method described in the paper [14]. For this purpose, after the hardness test, the sample was subjected to stress relief annealing at 270 °C for 2 hours. Annealing was performed in a vacuum furnace. Hardness test was performed again after annealing, near the same measurement points as before annealing. Residual stresses were calculated as the difference between the penetrator load for the sample with and without stress before and after annealing respectively, at the same depth of penetrator displacement. During the hardness tests, portion of elastic work was also determined as an area under the unloading curve.

During the hardness tests, the measurement system read the increasing loads as a function of indenter displacement. The measured hardness resulted from the maximum load on the indenter and the contact area of the indenter with the material surface. When loading the indenter, a reaction force was created which caused the nanoindenter frame to deflect. This deflection has been taken into account to correct the indenter displacement readings and thus minimize measurement errors. Also, in order to minimize measurement errors, the room temperature was stabilized to 21 °C ± 0.5 °C before starting the measurements.

3. Results and discussion

3.1. Results of the fatigue test

Fig. 5b presents the fatigue fracture of the drag strut eyelet with no laser processing. The drag strut was able to withstand 503 simulated landings and then cracked in its eyelet. The results of the fatigue tests carried out for drag strut without laser treatment of its eyelet have shown that fatigue cracks are located, with slight deviations, perpendicularly to the axle of the drag strut. They initiated on the nonmetallic inclusions and developed perpendicularly to the acting loads. In turn, the drag strut with laser processed eyelet was able to withstand 1701 simulated landings and then cracked at the weld between the eyelet and the sleeve of the drag strut (see Fig. 5a).

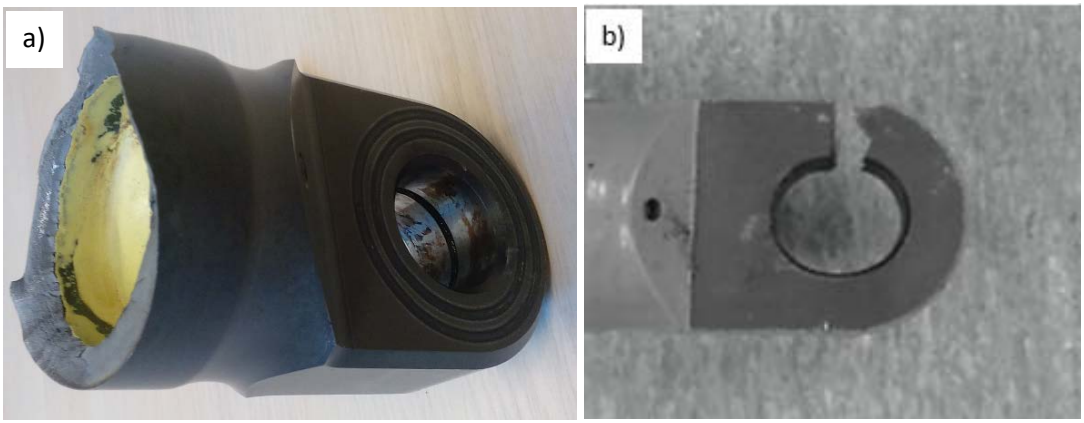

Fig. 5. View of the laser-treated eyelet (a) and untreated eyelet (b) – after fatigue tests.

3.2. Nanoindentation test results

In order to explain the causes of high fatigue resistance of the laser processed drag strut eyelet metallographic examinations and hardness test of the cross section of the eyelet, perpendicular to the axis of the drag strut, were performed. Hardness measurements were made before and after stress relief annealing along two lines as presented in the Fig. 4. Figs. 6 and 7 show results of hardness tests. The blue lines in Figs. 6 and 7 indicate the hardness of the material before laser processing (6 GPa). The results of the hardness test presented in Fig. 6 indicate that the hardness measured along “Line 1” is the highest at the laser processed surface and it reaches almost 12.5 GPa. As the distance from the laser processed surface increases, the hardness decreases. At a distance of about 500 μm from the surface, the hardness of the material is the same as the hardness of the material before the laser treatment and it is 6 GPa. In turn, hardness measured along “Line 2” at distance from the surface in the range of 15 μm to 915 μm is almost constant and it is about 6 GPa. A slightly higher hardness along “Line 2” was observed at a distance of 1 μm to 15 μm. Hardness at these distances from the surface is in the range of 5.3 GPa to 7 GPa. The high increase of the hardness of the laser-treated surface layer and the moderate increase of the hardness of the material between the melted paths cannot be the only cause of the increase of the fatigue resistance of the drag strut eyelet. In order to determine the elastic properties of the laser treated material and base metal nearby the processed area, during hardness measurements, the work of elastic deformation was also determined. Portion of elastic

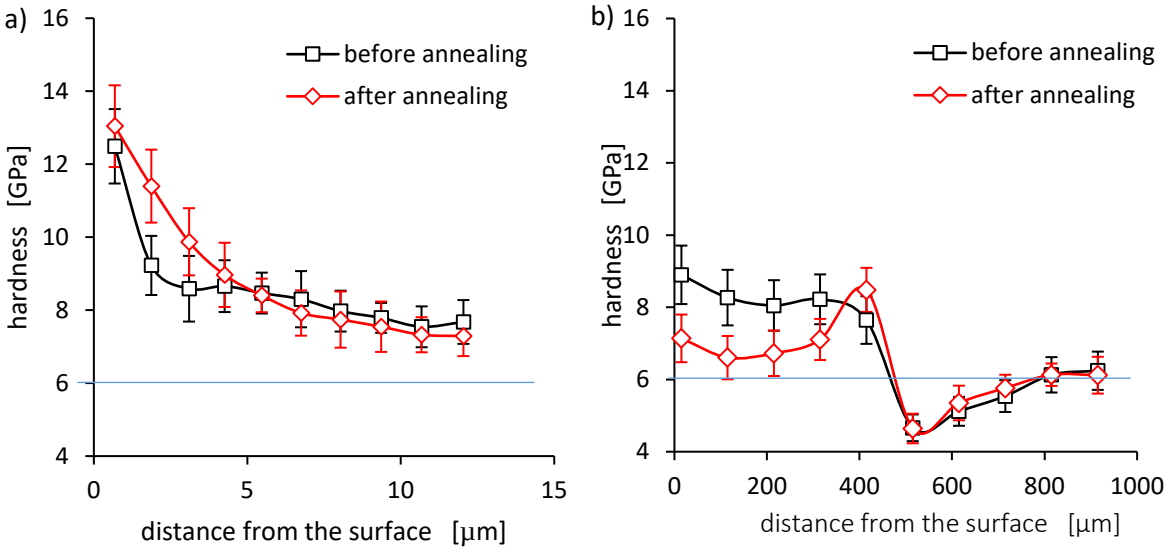

Fig. 6. Hardness profiles of laser treated LT steel before and after annealing along “Line 1” in the range from 0 to 13 µm (a), and in the range from 15 µm to 915 µm (b). Error bars represent ± standard deviation of five measurements.

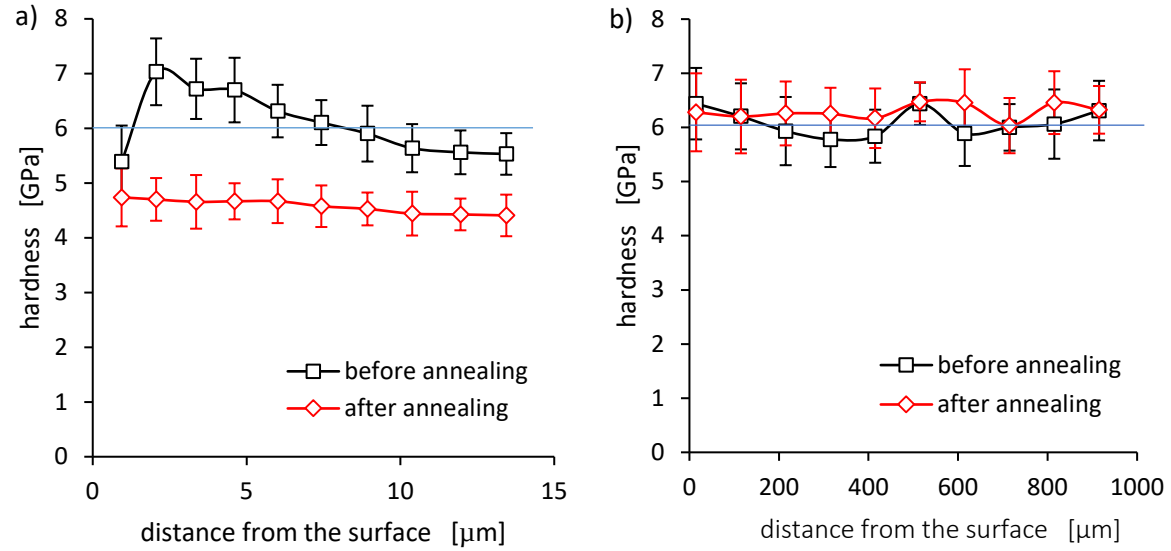

Fig. 7. Hardness profiles of base metal BM before and after annealing along “Line 2” in the range from 0 to 13 µm (a), and in the range from 15 µm to 915 µm (b). Error bars represent ± standard deviation of five measurements.

work for base metal was 18%. The blue lines in Figs 8 and 9 indicate the portion of elastic work of the material before laser processing. Figs 8 and 9 present portion of elastic work versus distance from the surface obtained for steel before and after stress relief annealing. As shown in Figs 8 and 9, laser treatment results in a strong increase in the elastic properties of both the material melted by the laser beam and the material between the melted paths. The high portion of elastic work of the melted material, reaching up to 38%, is observed at a distance up to 2 µm from the surface. Stress relief annealing does not reduce high-elastic properties in the surface

layer which is 5 μm thick. However, the increase in elastic properties of the processed material is observed up to a depth of about 500 μm. At greater depths, the elastic properties of the material were not increased in comparison to the base metal. In turn, the high portion of elastic

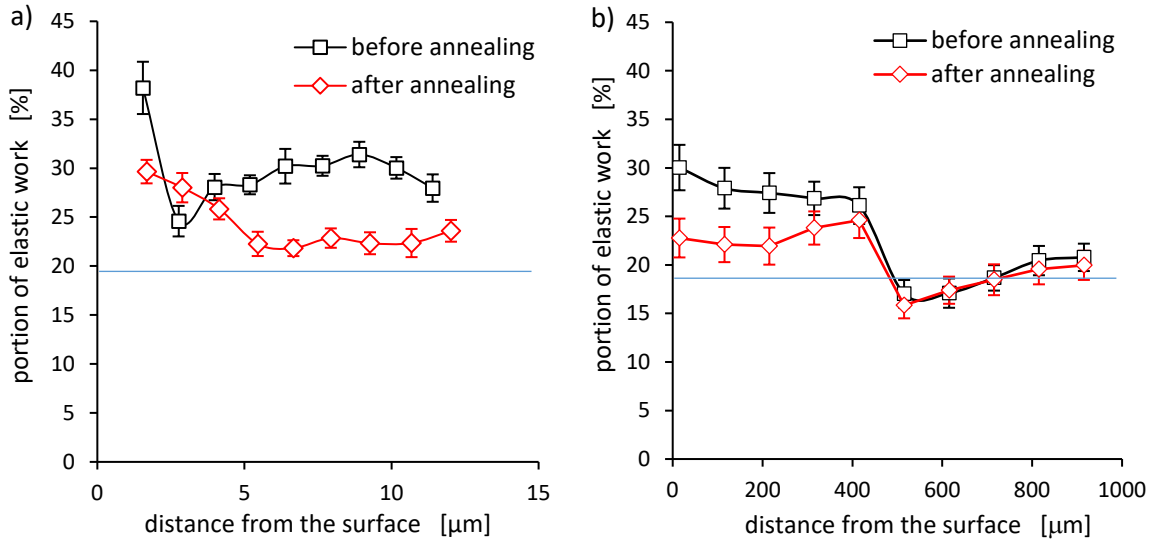

Fig. 8. Portion of elastic work profiles of laser treated LT steel before and after annealing along “Line 1” in the range from 0 to 13 μm (a), and in the range from 15 μm to 915 μm (b). Error bars represent ± standard deviation of five measurements.

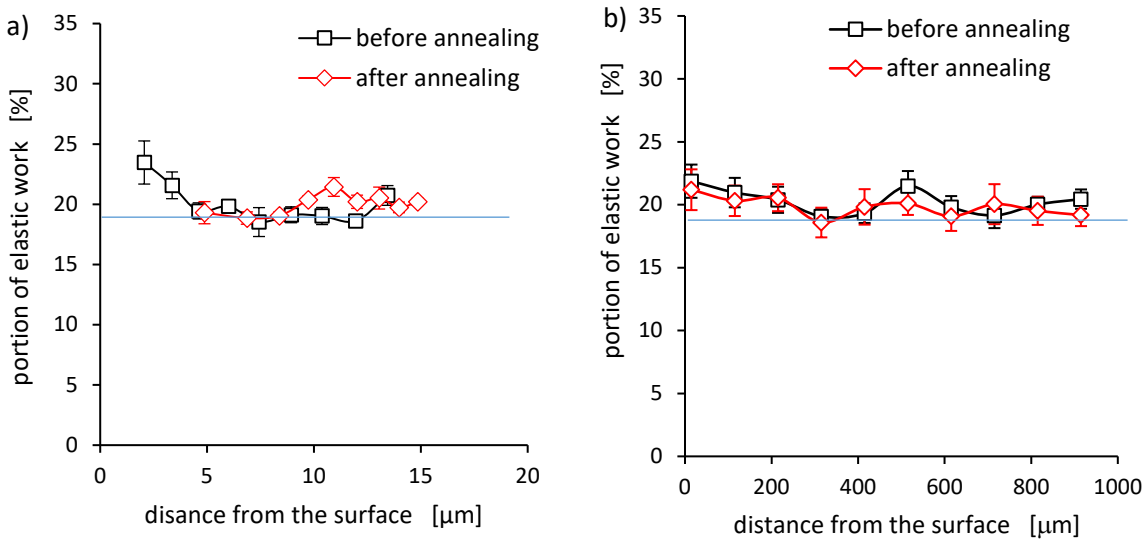

Fig. 9. Portion of elastic work profiles of base metal BM before and after annealing along “Line 2” in the range from 0 to 13 μm (a), and in the range from 15 μm to 915 μm (b). Error bars represent ± standard deviation of five measurements.

deformation for base metal located between melted paths occurs to a depth of about 5 μm. At this distance from the surface, the proportion of elastic work of the material is about 20%. This value does not change until the distance from the surface is 915 μm.

3.3. Results of residual stress measurements

3.3.1. Residual stress measured in nanoindentation test

The residual stress value can be calculated from the equation [14]:

$$\sigma_R = \frac{P^* - P_0}{A} \quad (1)$$

where:

P* – load of indenter in the stressed material (before annealing)

P_0 – load for the same displacement of indenter in the annealed material

A – contact area

Fig. 10 presents residual stress profile for two analysed lines obtained in multiple load cycle with increasing the load in the range from 100 mN up to 20 N, while Fig. 11 shows the results obtained on the cross section. As it can be seen in Fig. 10, high tensile residual stresses occur in the re-melted material. They reach 1870 MPa at a distance of approximately 1.6 μm from the surface and they decrease as the distance from the surface increases. At a distance of about 12 μm from the surface they reach a value of 0 and at greater distances they pass into compressive stresses. Compressive stresses along "Line 1" occur up to 350 μm from the surface to change subsequently into tensile stress. Tensile stress values at depths ranging from 350 μm to 915 μm vary from 0 GPa to 0.74 GPa.

Also, compressive stresses occur in the surface layer for the material between the re-melted paths. Maximal compressive stress along "Line 2" reaches 1660 MPa at the distance of 2 μm from the surface. Within 15 μm from the surface the residual stress is compressive nature, and then it changes to tensile stress. Tensile stresses occur up to a depth of 915 μm, and their values fluctuate in the range of 0 and 380 MPa.

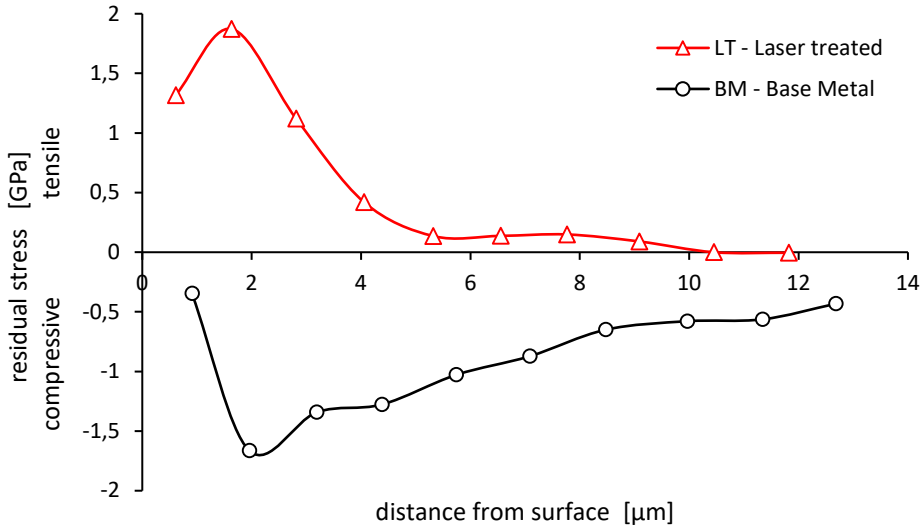

Fig. 10. Residual stress profiles along "Line 1" (LT) and "Line 2" (BM) in the range from 1 μm to 13 μm

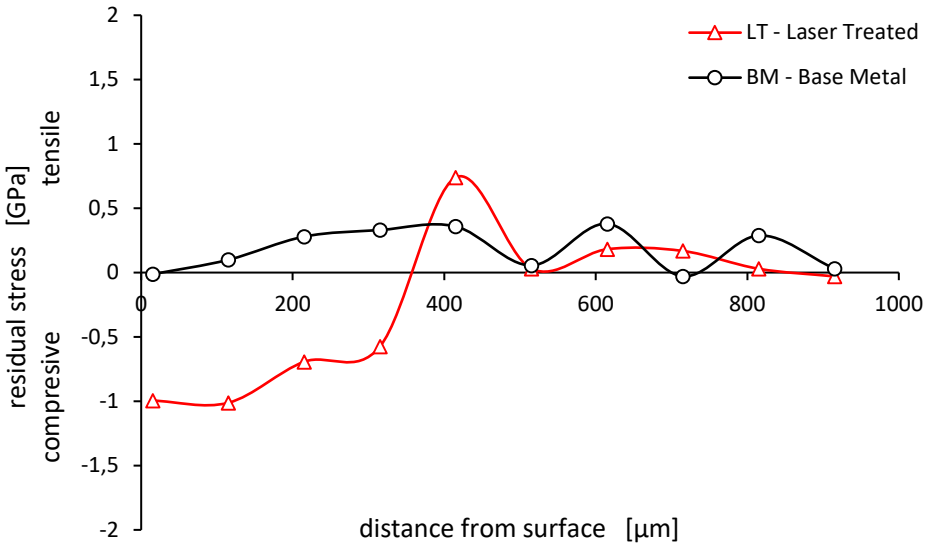

Fig. 11. Residual stress profiles along “Line 1” (LT) and “Line 2” (BM) in the range from 15 µm to 915 µm

3.3.2. Williamson-Hall analysis for crystallite size and residual stress measurement

X-Ray peak broadening is caused by deviation from the ideal crystalline lattice. Williamson-Hall method allow to separate the different contributions to specimen broadening (crystallite size and microstrain broadening of diffraction peaks). This analysis assumes that the peak profile is a convolution of the profiles from all of these contributions. Figs. 12a and 12b show XRD diffraction patterns for base metal, where Fig. 12a shows XRD pattern in the system of intensity vs. angle 2θ and Fig. 12b intensity vs diffraction vector K. Additionally Fig. 12b presents line broadening analysis performed using the Voigt function.

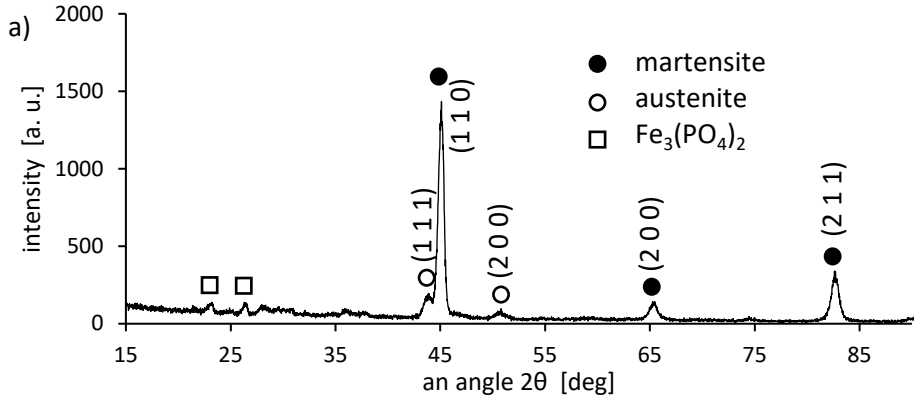

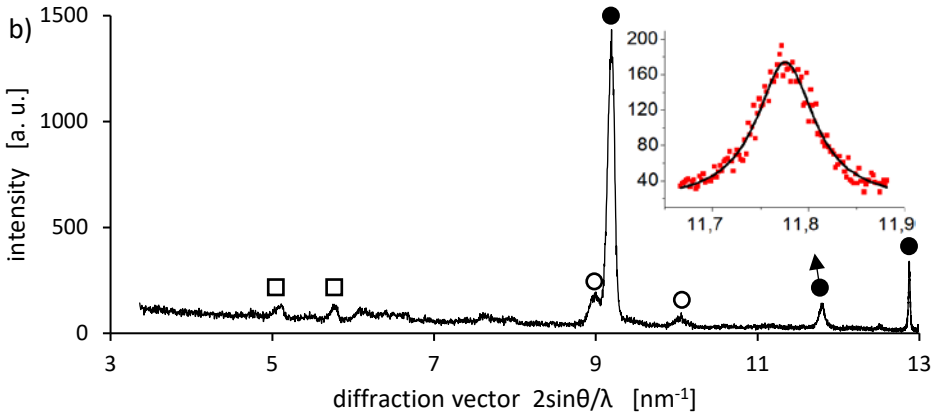

Fig. 12. XRD diffraction patterns for base material BM. The horizontal axis is based on the angle 2θ (a) and on the diffraction vector K (b). A diffraction peak fitted with a Voigt function is also shown.

The Williamson Hall method assumes that the total peak broadening is the sum of the broadening resulting from the size of the crystallites and the presence of microstrain [15]:

$$B = \frac{a_S \cdot \lambda}{L \cdot cos\theta} + 4\varepsilon \frac{sin\theta}{cos\theta} \tag{2}$$

or:

$$Bcos\theta = \frac{a_S \cdot \lambda}{L} + 4\varepsilon sin\theta \tag{3}$$

where: B is total broadening in radian, a_S is the Scherrer constant depends on the shape of the crystal, and the size distribution [16] (here is assumed to be 1), λ is an electron beam wavelength 0.15405 in nm, L is crystallite size represents a crystal portion with exactly the same crystallographic orientation such as sub-grains [17] in nm and ε is microstrain. Plots of $Bcos\theta$ vs. $sin\theta$ are presented in Fig. 13 and Table 2 summarizes the results of plots analysis. A modulus of elasticity equal to 201 GPa was used for calculating residual stress in martensite and austenite.

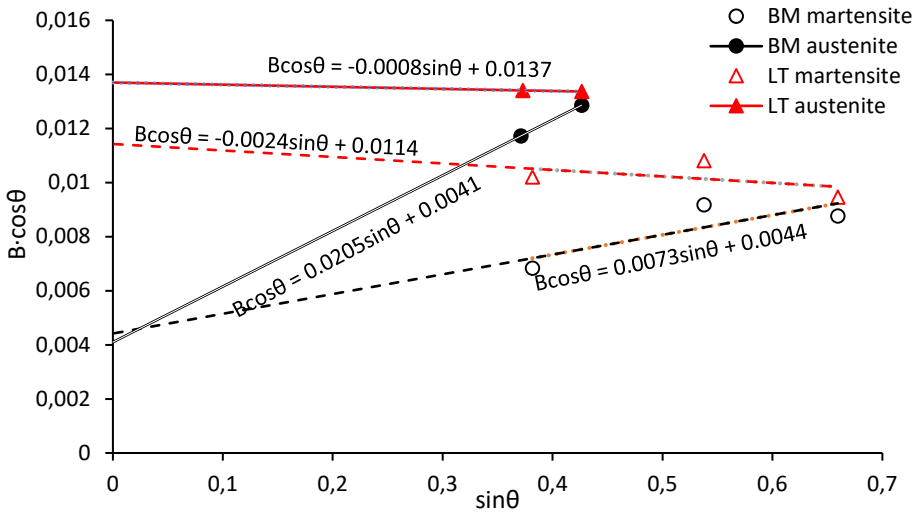

Fig. 13. Plots of Bcosθ vs. sinθ for base metal and for laser treated steel

Table. 2. Microstrain, crystallite size and residual stress in martensite and retained austenite for base metal and for laser hardened steel

Base Metal						Laser Treated					
martensite			austenite			martensite			austenite		
ε (-)	L (nm)	σ_R (MPa)	ε (-)	L (nm)	σ_R (MPa)	ε (-)	L (nm)	σ_R (MPa)	ε (-)	L (nm)	σ_R (MPa)
0.001825	35	370.5	0.00515	38	1045	-0.0006	14	-122		15	-41

Because the volume fraction of martensite and austenite was 84.5% and 14.5% for the base metal, and 86.2% and 13.8% for laser-melted steel, respectively, the total residual stress was calculated as a weighted average of residual stress for retained austenite and martensite. The total residual stress for base metal and for steel after laser treatment was 475 MPa and -111 MPa, respectively, where the minus indicates tensile stress.

4. Modified Williamson-Hall analysis for dislocation density calculation

Dislocations are as one of the major sources of lattice distortions, and their density can be determined on the basis of diffraction image analysis. The modified Williamson–Hall (MWH) method is known as an accessible method in XRD line profile analysis for dislocation density measurement [18]. For strong anisotropic materials as martensite, the MWH equation is written as follows [19]:

$$\Delta K \cong \frac{a_s}{L} + bM\sqrt{\frac{\pi}{2}\rho}\left(K\bar{C}^{1/2}\right) \tag{4}$$

where ΔK is the peak width (see Fig. 12b), a_s Scherrer constant as in equation (2), L is the crystallite size, b is the magnitude of the Burgers vector, M is a dimensionless constant and it is known as the dislocations distribution parameter, ρ is the dislocation density, K is the magnitude of the diffraction vector (see Fig. 12b), and $\bar{C}$ is dislocation contrast factor. In an untextured cubic polycrystalline material $\bar{C}$ is given by [20]:

$$\bar{C} = \bar{C}_{h00}(1 - qH^2) \tag{5}$$

where $\bar{C}_{h00}$ is the average dislocation contrast factor for the $\{h00\}$ reflections and is determined by the dislocation contrast factor for the $\{h00\}$ reflections of pure screw and pure edge dislocations as well as their fractions, q is a parameter that depends on the edge or screw character of the dislocations and H^2 is given by:

$$H^2 = \frac{h^2l^2+h^2k^2+l^2k^2}{(h^2+k^2+l^2)^2} \tag{6}$$

Equation (4) is a linear function $\Delta K = f(K\bar{C}^{1/2})$ and allows calculating the dislocation density from the slope of this line, assuming that the M parameter is known. In turn, the intersection of

this line with the ΔK axis determines the inverse of the size of the crystallites. To draw equation (4), it is necessary to know the factor $\bar{C}$ for each peak of the XRD pattern. According to equation (5), to determine the dislocation contrast factor $\bar{C}$ one needs knowledge of the dislocation contrast factor for the $\{h00\}$ reflections $\bar{C}_{h00}$ and the q parameter. To determine the parameter q, equation (4) should be substituted with equation (5). The following equation will then be obtained:

$$\frac{(\Delta K-\alpha)^2}{K^2} \cong \beta^2 \bar{C}_{h00}(1-qH^2) \tag{7}$$

where $\alpha = a_s/L$, $\beta = bM(\pi\rho/2)^{1/2}$. The experimental value of parameter q can be determined by imposing a linear relationship between the left - hand term and H^2 i.e. $(\Delta K-\alpha)^2/K^2 = f(H^2)$. Then, the inverse value of q is given by the intercept of the extrapolated line with the H^2 axis. Fig. 14 presents plot of equation (7) for martensite in BM and LT steel. In turn, the following equation is used to calculate the $\bar{C}_{h00}$ value for screw and for edge dislocations [21]:

$$\bar{C}_{h00_i} = a_i^{C_{h00}}\left[1-exp\left(\frac{-A}{b_i^{C_{h00}}}\right)\right] + c_i^{C_{h00}}A + d_i^{C_{h00}} \tag{8}$$

where the a_i^{Ch00}, b_i^{Ch00}, c_i^{Ch00}, and d_i^{Ch00} parameters (i is edge or screw) are determined by the elastic constants of the material and A is the elastic anisotropy parameter and is given as $A = 2C_{44}/(C_{11}-C_{12})$. For BCC crystals elastic parameters C_{11}, C_{12} and C_{44} are 230 GPa, 135 GPa and 116 GPa respectively [22]. Substitution of these values gives $A = 2.442$.

The remaining parameters needed to calculate $\bar{C}_{h00}$ separate for screw and for edge dislocations are given in Table 3. Finally the value of parameter $\bar{C}_{h00}$ is determined as a weighted average of parameter $\bar{C}_{h00i}$ for screw dislocations and $\bar{C}_{h00i}$ for edge dislocations, the weights being the fractions of these dislocations in the entire dislocation structure. To calculate the fractions of screw and edge dislocations in the material structure, the following equation is used [22]:

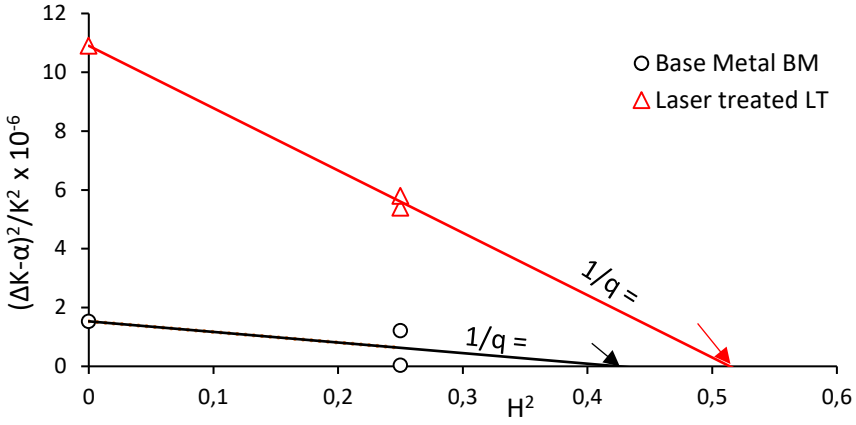

Fig. 14. Plot of equation (7) for martensite in BM and LT steel. The reciprocal of the intersect on the H^2 axis gives $1/q$.

$$f^{edge} = \frac{q^{th}_{screw} - q}{q^{th}_{screw} - q^{th}_{edge}} = 1 - f^{screw} \tag{9}$$

where f^{edge} and f^{screw} are the fraction of edge and screw dislocation respectively. In turn q^{th}_{screw} and q^{th}_{edge} means theoretical value of q for the pure screw or pure edge dislocations. These values can be obtained from [21]:

$$q_i^{th} = a_i^q \left[1 - exp\left(\frac{-A}{b_i^q}\right)\right] + c_i^q A + d_i^q \tag{10}$$

Parameter A is the same as in equation (8) and parameters a^q_i, b^q_i, c^q_i and d^q_i depend on elastic constants of the material and the dislocation slip systems activated in the crystal [21]. In cubic structures, the Burger vector of the prevailing dislocations is the shortest lattice vector. In bcc structure it is 1/2<111>. Parameters needed to calculate the parameter q are also listed in Table 3. In turn in Table 4, theoretical value of q for the pure screw or pure edge dislocations, the fraction of edge and screw dislocation, and the average dislocation contrast factor for the {h00} reflections for martensite in LT and BM are listed respectively.

Table 3. Parameters to calculate $\bar{C}_{h00}$ and q_i^{th} in BCC crystal

	Parameter q_i^{th}				Factor $\bar{C}_{h00}$			
	a^q_i	b^q_i	c^q_i	d^q_i	$a_i^{C_{h00}}$	$b_i^{C_{h00}}$	$c_i^{C_{h00}}$	$d_i^{C_{h00}}$
screw	8.659	0.3730	0.0424	-6.074	0.1740	1.9522	0.0293	0.0662
edge	7.2361	0.9285	0.1359	-5.7484	1.6690	21.124	0.0	0.0757

Table 4. Theoretical value of q, the fraction of edge and screw dislocation, and the average dislocation contrast factor for the {h00} reflections for martensite in LT and BM

	q^{th}_{screw}	q^{th}_{edge}	f^{edge}	f^{screw}	$\bar{C}_{h00screw}$	$\bar{C}_{h00edge}$	$\bar{C}_{h00average}$
LT mart.	2.686	1.298	0.53	0.47	0.119	0.258	0.192
BM mart.	2.686	1.298	0.23	0.77	0.119	0.258	0.150

Table 5 contains all values needed to plot MWH equation and Fig. 18. presents MWH plot. The dislocation density can be calculated from the slope of straight lines presented in Fig. 15 to the axis $K \cdot \bar{C}^{1/2}$ with the known parameter M. Taking the Burgers vector b = 0.284 nm [20] and the M parameter for tempered martensite lathe [20] M = 1.7 it is possible to calculate the martensite dislocation density for BM and LT steel, which is 1.84×10^{14} m^{-2} and 4.16×10^{13} m^{-2} respectively.

Table 5. Values needed to plot MWH equation

Laser Treated								Base Metal							
K	ΔK	h	k	l	H^2	q	$\bar{C}$	K	ΔK	h	k	l	H^2	q	$\bar{C}$
9.19	0.09	1	1	0	0.25	1.95	0.099	9.16	0.06	1	1	0	0.25	2.35	0.062
11.8	0.10	2	0	0	0	1.95	0.192	11.77	0.075	2	0	0	0	2.35	0.151
12.87	0.07	2	1	1	0.25	1.95	0.099	12.87	0.035	2	1	1	0.25	2.35	0.062

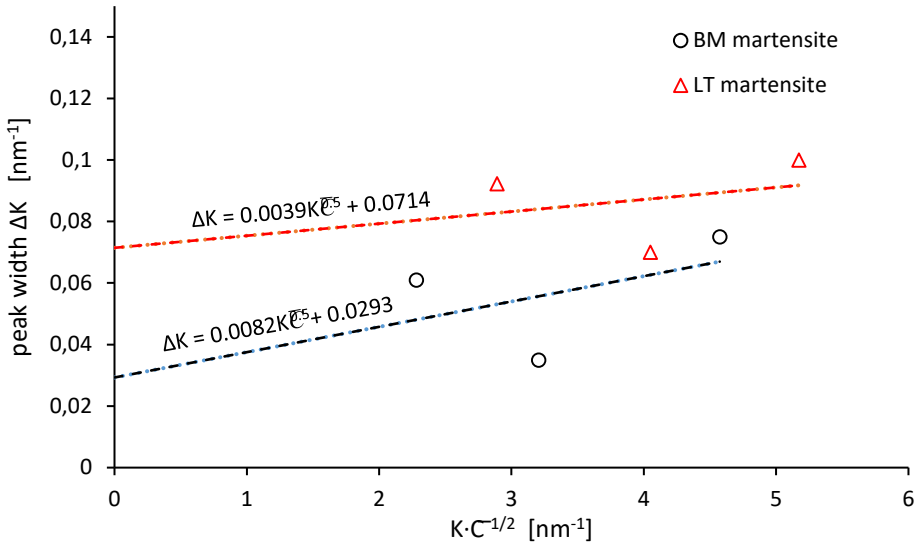

Fig. 15. The modified Williamson–Hall plot (ΔK versus $K\bar{C}^{1/2}$) for the martensite in base metal BM and laser treated LT steel.

5. Yield strength

Yield strength (σ_y) of lath martensite can be expressed as follows [24]:

$$\sigma_y = \sigma_0 + \sigma_{ss} + \sigma_{gb} + \sigma_\rho + \sigma_{pcpt} \tag{11}$$

where: σ_0 is contribution from Peierls-Nabarro stress and it is considered independent of solid solution strengthening by carbon, σ_{ss} is solid solution strengthening, σ_{gb} is sub-grain boundary strengthening, σ_ρ is the forest dislocation hardening term due to the presence of dislocations in lath boundaries and sub-block boundaries and σ_{pcpt} is the strength increment due to precipitation hardening. Jo et al. based on Rodriguez and Gutierrez's method [25] estimated σ_0 to be 201 MPa for a 0.3C lath martensite steel.

Solid solution strengthening σ_{ss} can be estimate based on alloy composition. Table 6, presents increment $\Delta\sigma_{ss}$ per 1 wt.% of alloying element. The effect of Ni as a solid solution strengthener has been omitted because of small atomic misfit between Ni and Fe. It was assumed also that most carbon would have precipitated during tempering. According to Hutchinson et al. [26] the content of carbon in interstitial solid solution is an approximately constant at a concentration in the range 0.01–0.03 wt% for as-quenched martensite (0.1–0.5 wt% C). In turn HajyAkbary et al. reported in their work that fraction of carbon in solid solution in the as-quenched and tempered 0.3% C steel was 0.05 wt%. The latter value was used for calculations of the solution strengthening of martensite due to carbon in the BM. In the case of laser processed steel, it was assumed that due to extremely high cooling speeds all carbon content remained in the solid, causing its solution strengthening.

Table. 6. Values needed to estimating solid solution strengthening contribution (MPa) [27].

element	Si	Mn	Cr	Cu	Ni	P	C
Δσ/wt.%	83	37	−30	38	0	470	4570

On the base of Tables 1 and 6, σ_{ss} for BM was estimated to be 354 MPa. In the case of steel melted with a laser beam, solution strengthening with carbon atoms and other alloying elements was calculated to be 1560 MPa.

Sub-grain boundary strengthening σ_{gb} can be calculated based on well-known Hall-Petch equation:

$$\sigma_{gb} = \frac{k_{HP}}{\sqrt{d_b}} \tag{12}$$

where k_{HP} is Hall–Petch slope and d_b is the effective grain size of martensite. Shibata et al. [28] reported that for block boundaries k_{HP} is given as 0.21 MPa·m^{½}. Determining the effective grain size of martensite is a problem. According to Daigne et al. [29] effective grain size of martensite means the lath width or the packet size. It can also be found in the literature that the prior-austenite grain size is taken as the effective grain size [27]. The fundamental principle of effective grain size is based on the interaction effect between dislocations and boundaries. The idea of effective grain size is associated with high-angle boundaries which are barriers hinder the movement of dislocations. Fig. 16a presents the prior-austenite grain size in martensitic microstructure of BM and high-angle boundaries in BM martensite are depicted in Fig. 16b. For the calculation of σ_{gb}, the lath width of martensite was taken, which in the case of BM was on average 0.80 μm. In turn, as a result of laser remelting, a cell structure with an average cell size of 50 nm was formed (Fig. 17). Considering the above-mentioned values, the sub-grain boundary strengthening σ_{gb} for BM and LT steel was calculated 235 MPa and 939 MPa, respectively. Dislocation hardening σ_{ρ} was calculated on the base of Taylor's model:

$$\sigma_{\rho} = \alpha M G b \sqrt{\rho} \tag{13}$$

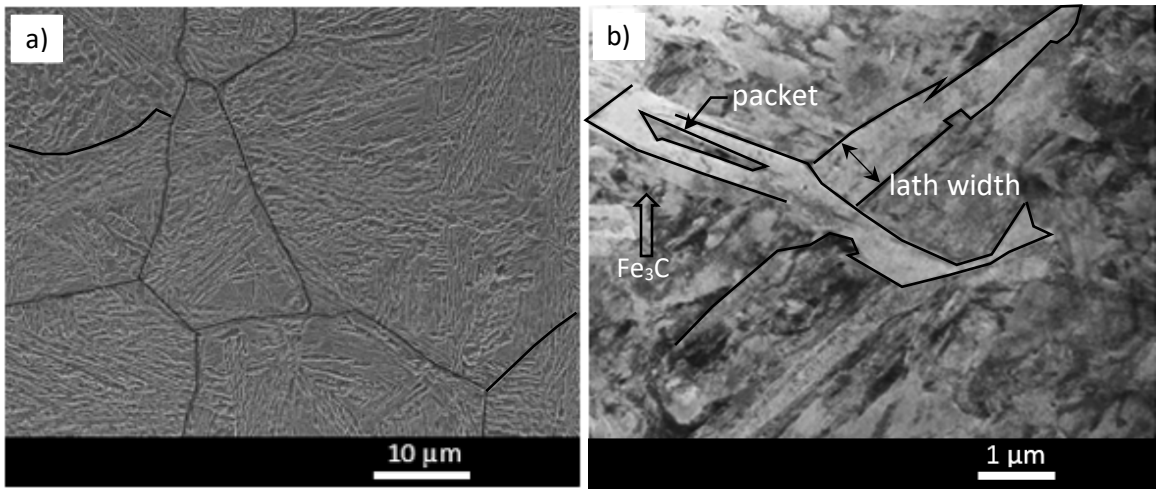

Fig. 16. SEM image (a) and TEM micrographs (b) of martensite in BM. In figure (a) the prior-austenite grain size is depicted by black line and in figure (b) high-angle boundaries in martensite are depicted.

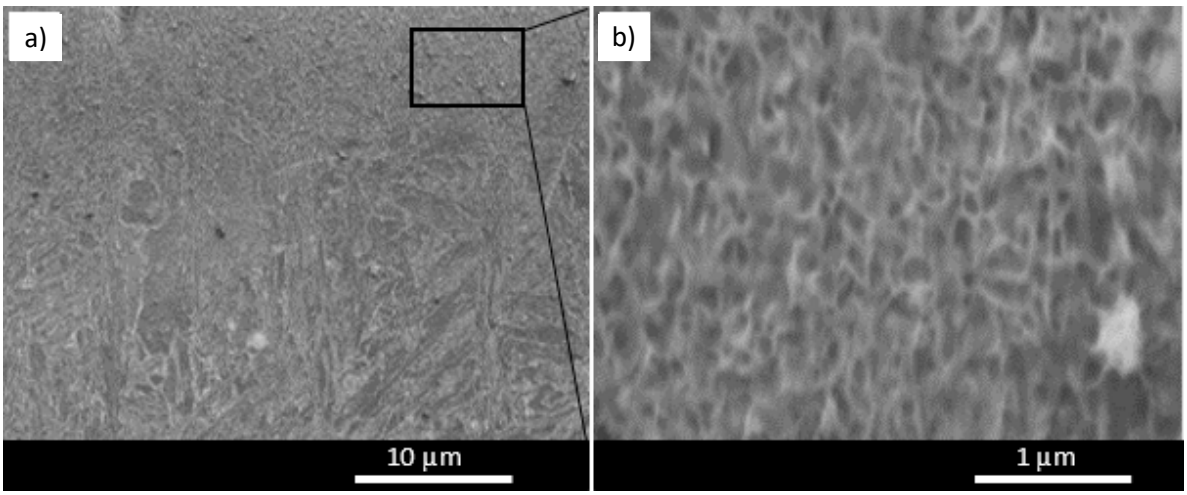

Fig. 17. SEM images of martensite in LT steel at a distance of 10 µm from the surface.

where α, M, G, b and ρ are the Taylor factor, a constant, the shear modulus, Burgers vector and dislocation density, respectively. Values $M = 1.7$, $\alpha = 0.35$, $G = 80$ GPa, $b = 0.284$ nm and $\rho_{BM} = 1.84 \times 10^{14}$ m^{-2} and $\rho_{LT} = 4.16 \times 10^{13}$ m^{-2} were taken to calculation dislocation hardening. Dislocation hardening σ_ρ for BM and LT steel is 183 MPa and 87 MPa respectively.

To calculate the strength increment due to precipitation hardening σ_{pcpt} the Ashby-Orowan equation was employed [27]:

$$\sigma_{pcpt} = \left(\frac{0.538Gb\sqrt{V_f}}{x}\right) ln\left(\frac{x}{2b}\right) \tag{14}$$

where V_f is the volume fraction of precipitates and x is the mean diameter of precipitates. As indicated by microscopic examination, there are two types of carbides, one was undissolved spherical carbide with slightly big size (see Fig. 16b) and the other, much smaller, with irregular shape, was precipitated carbide in tempering. The volume fraction of undissolved spherical

carbides is about 1.1% through measuring of five SEM images and their mean diameter was 140 nm (see Fig. 18). The volume fraction of equilibrium cementite at the tempering

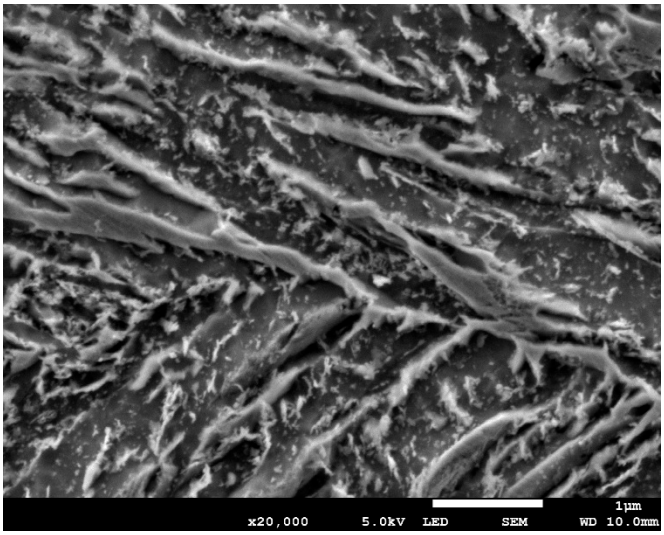

Fig. 18. SEM micrograph of base metal BM. Visible precipitation of carbides with irregular shapes, precipitated in tempering.

temperature (553 K) and tempering time (four hour) was determined as 0.03 from ThermoCalc software. Their mean diameter was assumed to be10 nm and this value is in line with reports from other authors [20]. Considering the above values, the precipitation strengthening caused by undissolved cementite and precipitated carbides during tempering was calculated on the basis of equation (14). The precipitation strengthening of undissolved carbides and carbide precipitation in tempering was 490 MPa and 134 MPa, respectively. In the case of laser-treated steel, microscopic examination did not reveal any precipitates, so that no precipitation strengthening occurred in this case. Fig. 19 shows the contribution of individual strengthening components to the yield strength of the base metal BM and alloy after laser processing LT.

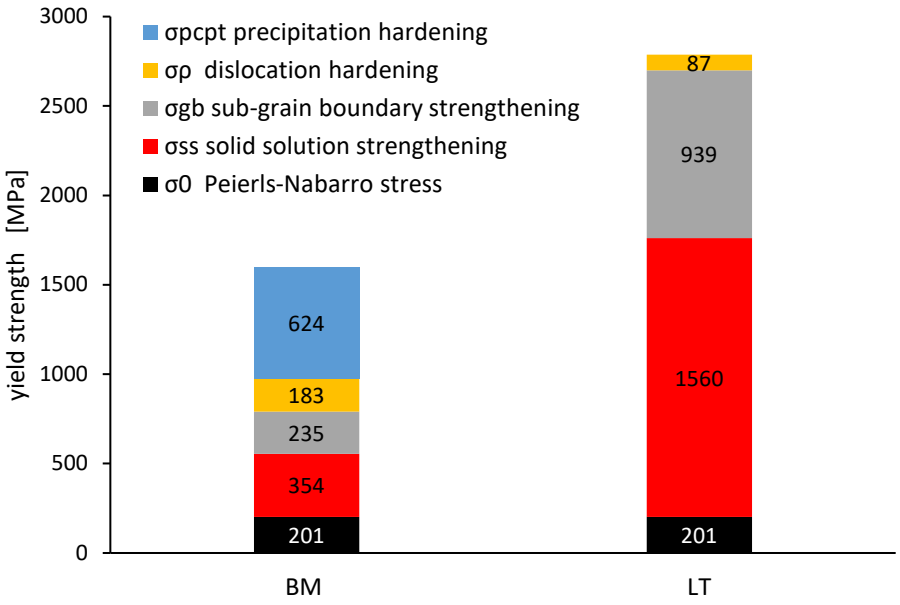

Fig. 19. Contribution of Peierls-Nabarro stress, solid solution, grain size, dislocation density and precipitation hardening on the yield strength of base metal BM and laser treated steel LT

As it results from Fig. 19 in the case of BM, the precipitation strength is almost 40% of the yield strength of material. After adding up all strengthening components, the yield strength of the base metal is 1587 MPa, which is consistent with the value obtained in the tensile test. For laser treated steel, the calculated yield strength is 2787 MPa, which is 75% higher compared to the base metal. About 90% of this value is obtained by solution strengthening and strengthening by sub-grain boundary.

6. Initiation of fatigue

Metallographic examination revealed that fatigue cracks initiated in the surface layer, at a non-metallic inclusion/metal matrix interface. In the case of the base metal, fatigue cracks initiated at a distance from the surface of 300 μm to 800 μm, i.e. in zones of tensile stress. At smaller distances from the surface, where high compressive stresses occurred, no fatigue cracks were noticed. After initiation, the cracks developed in a plane perpendicular to the acting stresses. In this way, cracks initiated at interface of the matrix and soft sulphides as well as at interface of the matrix and hard oxides, mainly Al_2O_3 and SiO_2. According to Lamagnere et al. [30] MnS sulphide hardness falls within a range from 3.2 GPa to 3.4 GPa which is significantly lower than that of the BM matrix. In turn aluminum oxide Al_2O_3 has hardness 32.2 GPa which is significantly higher. Some researchers believe that soft non-metallic inclusions such as manganese sulfides are more preferred than hard non-metallic inclusions such as aluminium oxides or silicon oxides. However, our observations show that fatigue cracks initiated both on hard and soft non-metallic inclusions (see Fig. 20). Possible cause of crack initiation was strong differences in elastic properties between non-metallic inclusions and the surrounding metallic matrix. Laser treatment increases the hardness and elastic properties of the metal matrix, which reduces the differences in hardness in relation to hard non-metallic inclusions, but at the same

time increases these differences in relation to soft sulphides. However, the increase in hardness of the metal matrix caused by laser processing is not large enough to achieve the hardness of hard oxides, which in consequence causes fatigue cracks to be initiated on both hard and soft non-metallic inclusions. Furthermore geometrically necessary dislocations may also form around non-metallic inclusions to facilitate plastic deformations accelerating the initiation of fatigue cracks. Figure 20a shows a crack in the base metal initiated at the metal matrix/manganese sulfide interface, at a distance of about 600 μm from the surface. A circumstance conducive to initiating this crack were also residual tensile stresses of about 380 MPa (see Fig. 11). Figure 20b shows a fatigue in the base metal initiated at the metal matrix/Al_2O_3 interface, at a distance of about 400 μm from the surface. As can be seen, in the presence of hard Al_2O_3 oxides, the dimensions of seat inclusions were larger than those of embedded inclusions. This may be due to the fact that after the debonding between the matrix and inclusions, friction wear of the softer matrix occurred.

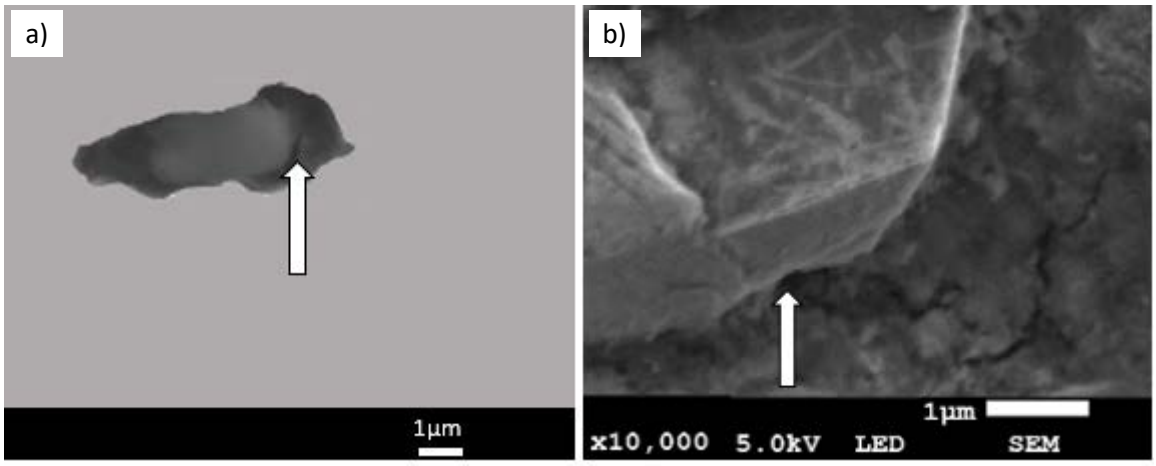

Fig. 20. Images showing initiating fatigue cracks on MnS (a) and aluminium oxide (b). The arrows indicate cracks developing perpendicular to the loads

In the case of areas melted with a laser beam, no fatigue cracks were observed, despite the occurrence of high tensile stresses reaching the value of about 1870 MPa, at a distance of 1.6 μm from the surface. This state of affairs should be seen in the fact that in the melted areas there were no non-metallic inclusions on which cracks could be initiated. The transition of the metal to the liquid state with the next extremely fast cooling caused the dissolution of non-metallic inclusions in solid solution. This in turn caused very strong solution strengthening of the matrix. In addition, remelting refined structure of the metal matrix (see Figs 17b) and further increased its yield point. As a result, matrix strengthening caused by remelting reached 2787 MPa, which is significantly more than the residual tensile stress generated by laser processing. What's more, melting steel with a laser beam caused an almost twofold increase in the elastic properties of the surface, which further contributed to the increase in fatigue resistance. At distances from the melted surface contained in the range from 15 μm to 350 μm, the structure was formed due to hardening from solid state. In this zone, laser processing generated favourable compressive stresses, which contributed to the increase in fatigue

resistance. In addition to the favourable residual compressive stresses in this zone, a much smaller grain of primary austenite was found, which further contributed to sub-grain strengthening of the matrix. Another factor favorably increasing the fatigue strength in the heat affected zone is the fact that solid state hardening from temperatures close to solidus temperature completely or partially dissolves non-metallic inclusions, which contributes to reducing their size. Murakami et. al [31] [32] have investigated the effects of inclusions on fatigue strength of high-strength steels and have expressed the fatigue limit as functions of Vickers hardness *HV* (Kgf/mm^2) and the square foot of the projection area (μm) of an inclusion. The fatigue limit prediction equation proposed by Murakami is as follows:

$$\sigma_w = \frac{1.41(HV+120)}{\left(\sqrt{area_{max}}\right)^{1/6}}\left[\frac{(1-R)}{2}\right]^{\alpha} \tag{15}$$

where R is stress ratios (the minimum stress to the maximum stress) and $\alpha = 0.226 + HV \times 10^{-4}$. As follows from equation (15), reducing the size of non-metallic inclusions and increasing the hardness of the matrix contributes to the increase in fatigue resistance of the material.

In the case of the base metal BM located between two concentrically melted paths at a distance from the surface of up to 15 μm there are high residual compressive stresses. The maximum value of these stresses is 1663 MPa and they occurs at a distance from the surface of 2 μm.

The maximum normal stresses due to fatigue between melted paths can be calculated from the equation:

$$\sigma = \frac{P}{2b \cdot h} + \frac{6M_0}{b \cdot h^2} \tag{16}$$

where P is maximal load (195.4 kN), b is cross section width (b = 25 mm), h is the height of the cross-section (h = 16 mm), and M_0 is maximal moment acting on the cross-section. This moment can be calculated from:

$$M_0 = P \cdot R \cdot \left(\frac{1}{2} - \frac{1}{\pi}\right) \tag{17}$$

where R is the average radius at which the force P is acting (R = 21.5 mm). After substituting the values for equation (16), the maximum stress due to fatigue loading between melted paths is 715 MPa. This stress is of the tensile type. The occurrence of non-metallic inclusions in the material structure between the melted paths causes stress concentrations. However, the stresses concentrated on non-metallic inclusions do not exceed the value of 3180 MPa, i.e. the sum of the yield stress of the material and the residual stresses.

As a consequence of such high residual compressive stresses, no fatigue cracks were observed in this zone. At distances from surfaces greater than 15 μm, residual stresses change the sign and turn into tensile stresses. In the range from 15 μm to 915 μm, the value of these stresses oscillates from 0 MPa to 378 MPa. However, fatigue cracks usually initiate on the surface or in areas just below the surface, therefore residual tensile stresses occurring at distances from the surface above 15 μm do not significantly reduce the fatigue strength of material located between melted paths.

7. Conclusion

In this research the laser treated eyelet of undercarriage drug strut made of a lath martensitic steel in the as-quenched and tempered conditions is evaluated. The laser treatment consisted of two re-melted and concentric paths with diameters 39 mm and 47 mm. Laser processing concentrated on both sides around the hole of eye. Residual stresses in the laser-treated steel (LT) and in the base metal (BM) located between the melted paths were determined using a nanoindentation test and analysis of diffraction pattern using the Williamson Hall method. Additionally, dislocation density in both examined areas of the eyelet was determined using modified Williamson Hall analysis. The following conclusions are drawn as follows:

1. Laser treatment causes strong solution strengthening and sub-grain strengthening of melted material, which causes a 75% increase in yield point compared to base metal and at the same time, laser processing increases the hardness almost two-fold and the elastic properties of the surface almost double.
2. Laser surface remelting generates strong residual tensile stresses in the processed steel to a depth of up to 15 μm. The highest value of these stresses is 1870 MPa at a distance of 1.6 μm from the treated surface. At the same distance from the surface in the base metal located between the melted paths, the greatest compressive residual stresses occur. Their value is 1663 MPa at a distance of 2 μm from the surface. These residual stresses contribute to suppressing the initiation of fatigue cracks in base metal.
3. Laser treatment dissolves non-metallic inclusions in the melted material, which contributes to an increase in fatigue resistance because cracks initiate on non-metallic inclusions.
4. The dislocation strengthening is two times higher for base metal than for laser-melted areas.
5. Both methods used to determine residual stresses in the examined eyelet areas, i.e. nanoindentation test and Williamson Hall analysis, give similar and comparable results.

Acknowledgment

The authors would like to thank Jerzy Doberski for his help in performing laser beam processing of undercaridge drug strut and Grzegorz Gajowiec for performing investigation and analysis using SEM.

Funding

Not applicable.

Author information
Affiliations
Gdańsk University of Technology, Mechanical Engineering Faculty, Gdańsk, G. Narutowicza 11/12, 80-233 Gdańsk, Poland
Marek Szkodo & Alicja Stanisławska

Geoengineering Faculty, University of Warmia and Mazury in Olsztyn**,** Michała Oczapowskiego 2, 10-719 Olsztyn, Poland
Anna Bień

Corresponding author
Correspondence to Marek Szkodo.

Ethics declarations
Conflict of interest
The authors declare that they have no conflict of interest.

References
1. Woo, W.-S., & Lee, C.-M. A Study on the Optimum Machining Conditions and Energy Efficiency of a Laser-Assisted Fillet Milling. International Journal of Precision Engineering and Manufacturing-Green Technology. 2018; 5(5):593-604.
2. Lee, C.-M., Kim, D.-H., Baek, J.-T., & Kim, E.-J. Laser assisted milling device: A review. International Journal of Precision Engineering and Manufacturing-Green Technology, 2016; 3(2):199-208.
3. Lee, C.-M., Kim, D.-H., Baek, J.-T., & Kim, E.-J. Laser assisted milling device: A review. International Journal of Precision Engineering and Manufacturing-Green Technology. 2016; 3(2):199-208.
4. Černý I, Sís J. Fatigue Strength of Laser Hardened 42CrMo4 Steel Considering Effects of Compressive Residual Stresses on Short Crack Growth. Procedia Engineering. 2014;74:417-20.
5. Božić Ž, Schmauder S, Wolf H. The effect of residual stresses on fatigue crack propagation in welded stiffened panels. Engineering Failure Analysis.
6. McDaniels RL, White SA, Liaw K, Chen L, McCay MH, Liaw PK. Effects of a laser surface processing induced heat-affected zone on the fatigue behavior of AISI 4340 steel. Materials Science and Engineering: A. 2008;485:500-7.
7. De la Cruz P, Odén M, Ericsson T. Effect of laser hardening on the fatigue strength and fracture of a B–Mn steel. International Journal of Fatigue. 1998;20:389-98.
8. Bergmann HW. Current Status of Laser Surface Melting of Cast Iron. Surface Engineering. 1985;1:137-56.
9. Walker KF, Lourenço JM, Sun S, Brandt M, Wang CH. Quantitative fractography and modelling of fatigue crack propagation in high strength AerMet®100 steel repaired with a laser cladding process. International Journal of Fatigue. 2017;94, Part 2:288-301.
10. Lourenço JM, Sun SD, Sharp K, Luzin V, Klein AN, Wang CH, Brandt M. Fatigue and fracture behavior of laser clad repair of AerMet® 100 ultra-high strength steel. International Journal of Fatigue. 2016;85:18-30.
11. BieŃ A, Szkodo M, Doberski J, KarpiŃSki B. Effect of selective laser treatment on initiation of fatigue crack in the main part of an undercarriage drag strut. Chinese Journal of Aeronautics. 2019;32:701-14.

12. Szkodo M, Bien A. Influence of laser processing of the low alloy medium carbon structural steel on the development of the fatigue crack. Surface & Coatings Technology. 2016;296:117-23.
13. Bień A, Kłysz S, inventorsMethod to block the propagation of fatigue cracks (in Polish). Poland2012.
14. Lee Y-H, Dongil K, inventorsResidual stresses in DLC/Si and Au/Si systems: Application of a stress relaxation model to the nanoindentation technique2002.
15. Williamson GK, Hall WH. X-ray line broadening from filed aluminium and wolfram. Acta Metallurgica. 1953;1:22-31.
16. Scherrer P. Bestimmung der inneren Struktur und der Größe von Kolloidteilchen mittels Röntgenstrahlen. In: Zsigmondy R, editor. Kolloidchemie Ein Lehrbuch. Berlin, Heidelberg: Springer Berlin Heidelberg; 1912. p. 387-409.
17. Khoshkhoo MS, Scudino S, Thomas J, Surreddi KB, Eckert J. Grain and crystallite size evaluation of cryomilled pure copper. Journal of Alloys and Compounds. 2011;509:S343-S7.
18. Ungár T, Borbély A. The effect of dislocation contrast on x-ray line broadening: A new approach to line profile analysis. Applied Physics Letters. 1996;69:3173-5.
19. Révész Á, Ungár T, Borbély A, Lendvai J. Dislocations and grain size in ball-milled iron powder. Nanostructured Materials. 1996;7:779-88.
20. HajyAkbary F, Sietsma J, Böttger AJ, Santofimia MJ. An improved X-ray diffraction analysis method to characterize dislocation density in lath martensitic structures. Materials Science and Engineering: A. 2015;639:208-18.
21. Ungar T, Dragomir I, Revesz A, Borbely A. The contrast factors of dislocations in cubic crystals: the dislocation model of strain anisotropy in practice. Journal of Applied Crystallography. 1999;32:992-1002.
22. Cong Z, Murata Y. Dislocation Density of Lath Martensite in 10Cr-5W Heat-Resistant Steels. MATERIALS TRANSACTIONS. 2011;52:2151-4.
23. Kunieda T, Nakai M, Murata Y, Koyama T, Morinaga M. Estimation of the System Free Energy of Martensite Phase in an Fe-Cr-C Ternary Alloy. ISIJ International. 2005;45:1909-14.
24. Kim B, Boucard E, Sourmail T, San Martín D, Gey N, Rivera-Díaz-del-Castillo PEJ. The influence of silicon in tempered martensite: Understanding the microstructure–properties relationship in 0.5–0.6wt.% C steels. Acta Materialia. 2014;68:169-78.
25. Jo K-R, Seo E-J, Hand Sulistiyo D, Kim J-K, Kim S-W, De Cooman BC. On the plasticity mechanisms of lath martensitic steel. Materials Science and Engineering: A. 2017;704:252-61.
26. Hutchinson B, Hagström J, Karlsson O, Lindell D, Tornberg M, Lindberg F, Thuvander M. Microstructures and hardness of as-quenched martensites (0.1–0.5%C). Acta Materialia. 2011;59:5845-58.
27. Wang Y, Sun J, Jiang T, Sun Y, Guo S, Liu Y. A low-alloy high-carbon martensite steel with 2.6 GPa tensile strength and good ductility. Acta Materialia. 2018;158:247-56.
28. Shibata A, Nagoshi T, Sone M, Morito S, Higo Y. Evaluation of the block boundary and sub-block boundary strengths of ferrous lath martensite using a micro-bending test. Materials Science and Engineering: A. 2010;527:7538-44.
29. Daigne J, Guttmann M, Naylor JP. The influence of lath boundaries and carbide distribution on the yield strength of 0.4% C tempered martensitic steels. Materials Science and Engineering. 1982;56:1-10.
30. Lamagnere P, Girodin D, Meynaud P, Vergne F, Vincent A. Study of elasto-plastic properties of microheterogeneities by means of nano-indentation measurements: Application to bearing steels. Materials Science and Engineering: A. 1996;215:134-42.
31. Murakami Y, Kodama S, Konuma S. Quantitative evaluation of effects of non-metallic inclusions on fatigue strength of high strength steels. I: Basic fatigue mechanism and evaluation of correlation between the fatigue fracture stress and the size and location of non-metallic inclusions. International Journal of Fatigue. 1989;11:291-8.

32. Murakami Y, Usuki H. Quantitative evaluation of effects of non-metallic inclusions on fatigue strength of high strength steels. II: Fatigue limit evaluation based on statistics for extreme values of inclusion size. International Journal of Fatigue. 1989;11:299-307.